Delft University of Technology

Biodegradation of Oxide Nanoparticles in Apoferritin Protein Media

A Systematic Electrochemical Approach

Rahimi, Ehsan; Kim, Donghoon; Offoiach, Ruben; Sanchis-Gual, Roger; Chen, Xiang Zhong; Taheri, Peyman; Gonzalez-Garcia, Yaiza; Mol, Johannes M.C.; Fedrizzi, Lorenzo; Pané, Salvador

Important note
To cite this publication, please use the final published version (if applicable).
Please check the document version above.

RESEARCH ARTICLE

ADVANCED
MATERIALS
INTERFACES
Open Access

www.advmatinterfaces.de

Check for updates

Biodegradation of Oxide Nanoparticles in Apoferritin Protein Media: A Systematic Electrochemical Approach

Ehsan Rahimi,* Donghoon Kim, Ruben Offoiach, Roger Sanchis-Gual,*
Xiang-Zhong Chen, Peyman Taheri, Yaiza Gonzalez-Garcia, Johannes M. C. Mol,
Lorenzo Fedrizzi, Salvador Pané,* and Maria Lekka*

Functional oxide nanoparticles are extensively utilized in the last decades for biomedical purposes due to their unique functional properties. Nevertheless, their biodegradation mechanism by biological species, particularly by proteins at oxide/protein interfaces, still remains limited. Here, a systematic approaches is provided to investigate electrochemical behavior, electronic properties, and biodegradation mechanism of cobalt ferrite (CFO) and cobalt ferrite-bismuth ferrite (CFO-BFO) core-shell nanoparticles in apoferritin-containing media. Scanning Kelvin probe force microscopy results indicate that the presence of a thin shell ($\approx$5 nm) of BFO on CFO causes a significant increase in surface potential. The potentiodynamic polarization measurements in different solutions showed higher anodic current densities for both samples when decreasing pH and increasing apoferritin concentration. Notably, CFO-BFO exhibits lower anodic current densities than CFO due to a slightly higher flat band potential and lower donor density distribution on CFO-BFO than on CFO, which results in lower electrochemical activity. Long-term monitoring reveals that biodegradation of both nanoparticles is accelerated by high apoferritin concentrations and acidic media, resulting in the decrease of electrochemical potentials and impedance values, and enhancement of metal ion release. Thus, this systematic biodegradation study can help to predict the lifespan and toxicity of these functional nanoparticles in biological environments.

1. Introduction

The development of various synthesis methods for functional oxide nanostructures with unique properties has led to significant advances in biomedical applications of nanostructures as desired functionalities and morphologies can be designed.[1,2] Among various oxide nanomaterials, magnetic oxide nanostructures have been suggested for targeted drug delivery,[3–6] tissue engineering,[7–9] magnetic hyperthermia treatment,[10–13] and magnetic resonance imaging[14–16] since the magnetic properties can be wirelessly controlled with external magnetic fields, which is well known to be harmless to the human body organs. Lately, magnetoelectric core-shell nanoparticles also emerged as attractive materials since electrical stimulation can be triggered by the application of external magnetic fields, which enable the use of these nanoparticles for targeted drug deliveries and cell stimulation/proliferation.[17–19] Among them, spinel ferrites as cobalt ferrite ($CoFe_2O_4$, CFO) nanoparticles have gained particular scientific and technological interest and are extensively utilized in several branches of engineering and medicine due to their magnetic and catalytic properties, mechanical hardness, and chemical stability, among others.[20–23] Furthermore, by compositing the CFO or creating core-shell nanoparticles by covering it with multiferroic materials such as bismuth ferrite ($BiFeO_3$, BFO) into CFO-BFO, we can achieve novel

E. Rahimi, R. Offoiach, L. Fedrizzi
Polytechnic Department of Engineering and Architecture
University of Udine
Udine 33100, Italy
E-mail: e.rahimi-2@tudelft.nl

E. Rahimi, P. Taheri, Y. Gonzalez-Garcia, J. M. C. Mol
Department of Materials Science and Engineering
Delft University of Technology
Delft 2628 CD, The Netherlands

D. Kim, R. Sanchis-Gual, X.-Z. Chen, S. Pané
Multi-Scale Robotics Lab (MSRL)
Institute of Robotics & Intelligent Systems (IRIS)
ETH Zurich
Zurich 8092, Switzerland
E-mail: rsanchis@ethz.ch; vidalp@ethz.ch

M. Lekka
CIDETEC
Basque Research and Technology Alliance (BRTA)
Donostia-San Sebastián 20014, Spain
E-mail: mlekka@cidetec.es

**ADVANCED
SCIENCE NEWS**

www.advancedsciencenews.com

**ADVANCED
MATERIALS
INTERFACES**
Open Access

www.advmatinterfaces.de

multifunctionalities including magnetoelectric, magnetooptic, and photocatalytic properties.[24,25]

Although there have been many efforts to enhance their biocompatibility, control drug targeting, and efficiently release therapeutics by modifying the surfaces or compositions of magnetic nanoparticles,[26,27] studies on their other important aspects, such as biodegradation, metal ion release, and remediation mechanisms in contact with different proteins, cells, or macrophages are still lacking.[28,29] It is worth noticing that the release of metal ions (such as Cu^{2+}, Co^{3+}, Ni^{2+}, Fe^{2+}, etc.,) from nanomaterials can induce the generation of reactive oxygen species (ROS), and toxic responses, which trigger cytotoxicity, inflammations, oxidative stress, and oxidation of protein molecules.[30,31] In particular, oxidative stress can happen in the lungs, kidneys, and liver of the human body[32,33] due to the released metal ions from iron oxide and cobalt-ferrite nanoparticles. In these parts of the human body, apoferritin and ferritin (apoferritin filled with a metal complex core) proteins undoubtedly play a substantial role in the metal ion-release and/or up-taking process of magnetic nanoparticles.[33–35]

Intracellular degradation and physiological remediation processes by ferritin proteins, in which proteins uptake Fe^{2+} or Co^{2+} ions, have been studied in vitro and in vivo using scanning transmission electron microscopy (STEM),[33] energy-dispersive X-ray spectroscopy (EDXS),[34,36] inductively coupled plasma (ICP),[30,37] and monitoring the magnetic response[29,38] for iron- and cobalt-containing nanoparticles.[39–41] However, more systematic studies and advanced characterization methods are required in order to understand the kinetics and thermodynamic interactions, specific electronic properties, and electrochemical responses at protein nanobiofilm and oxide surface interfaces. Elucidating degradation and/or biodegradation and remediation mechanisms would allow for a more bespoke design and development of functional oxide nanostructures with minimal toxicity and maximized efficiency.[26,42]

Hence, in this research, we report new insights into electrochemical interactions, electronic properties, and biodegradation mechanism of both CFO and CFO@BFO nanoparticles during their exposure to phosphate-buffered saline (PBS) with various concentrations of apoferritin protein (0, 10, 100 µg mL^{-1}) and pH (7, 5, and 3) values. To achieve these goals, a combination of multi-techniques characterization was utilized. Using scanning Kelvin probe force microscopy (SKPFM), we examined the effect of a thin layer of coated BFO on the surface potential difference and/or surface charge distribution. Electrochemical measurements, including the potential versus time (E-t), potentiodynamic polarization, electrochemical impedance spectroscopy (EIS), and Mott-Schottky analyses, were used to elucidate the electrochemical current-potential response of both nanoparticles, their total impedance value or resistance to charge transfer, and especially their electronic properties. These techniques provide important information about the interaction between the nanoparticles and apoferritin, shedding light on the biodegradation processes. Therefore, this work offers new approaches to acquiring a comprehensive understanding of the biodegradation processes of oxide nanoparticles for their application in the human physiological media.

2. Results and Discussion

2.1. Physical and Electronic Characterization of CFO and CFO-BFO Nanoparticles

The functional $CoFe_2O_4$ (CFO) core particles were synthesized by co-precipitation and hydrothermal methods, and the $BiFeO_3$ (BFO) shell was synthesized using a sol-gel method (Experimental Section). Their crystalline structures and morphologies were analyzed by X-ray diffraction (XRD) and transmission electron microscopy. As previously reported,[24] the CFO core exhibits a Fd-3m spinel structure while the BFO shell has a R3c rhombohedral structure without any secondary phases or impurities (**Figure 1**a). Both CFO and CFO-BFO nanoparticles show narrow size distributions (Figure 1b,c) with a mean size of ≈20–30 nm. The core-shell nature of CFO-BFO (Figure 1d–g) was confirmed by EDXS mapping, where Bi ions are localized in the shell area while Co ions are concentrated in the particle center.

For materials in contact with various ions and reactive species such as proteins and cells, the reactivity or the degradability of the materials is determined by the energy state of valence band electrons.[43] In this regard, the surface potential or work function (WF) can be used as indicator of the chemical stability of the materials.[44] Surface potential refers to the electric potential at the surface of a material, while WF indicates the minimum energy required to remove an electron from the material's surface. Thus, materials with high surface potential or WF are supposed to have higher stability of valance electrons, which inhibit them from participating in electrochemical reactions.[44–46] Therefore, to determine the local surface potential on the surface of both nanoparticles, we employed AFM and SKPFM surface analysis (**Figure 2**). Both CFO and CFO-BFO nanoparticles exhibited a lower response to electrostatic interactions (lower surface potential/charge) in comparison with the glassy carbon substrate, which is attributed to a combination of the local changes in polarization, bandgap energy values, and density of states distribution.[47] Considering that both samples have a similar roughness, the surface potential line profiles clearly show that the CFO-BFO nanoparticles exhibit a higher surface potential difference (ΔP) to the glassy carbon substrate (ΔP = ≈34 mV) than that of CFO nanoparticles (ΔP = ≈22 mV) (Figure 2c,f). Note that surface potential/charge values were extracted from both samples at the same height to ensure their comparison. Accordingly, the CFO nanoparticles exhibit a higher semiconductive behavior (electrons (Fe^{2+}) or electron holes (Co^{3+}) and obtain n-or p-type semiconductivity) than the CFO-BFO, which is in agreement with other research groups' results on current sensing AFM.[48] In addition, since the bandgap energy value of CFO-BFO core-shell nanoparticles (E_g = ≈1.8 eV) is higher than that of CFO nanoparticles (E_g = ≈1.45 eV),[49] the CFO nanoparticles show a lower barrier to the transfer of electrons from valance band energy (E_v) to conduction band energy (E_c). Note that, the electron transfer mechanism for both nanoparticles is based on electron hopping between iron or cobalt ions due to the smaller activation energy and lower bandgap energy for the transfer process.[50,51]

It is important to mention that the interface between CFO and BFO shell can lead to a special density of states and electronic structure (characterized by the presence of additional states at
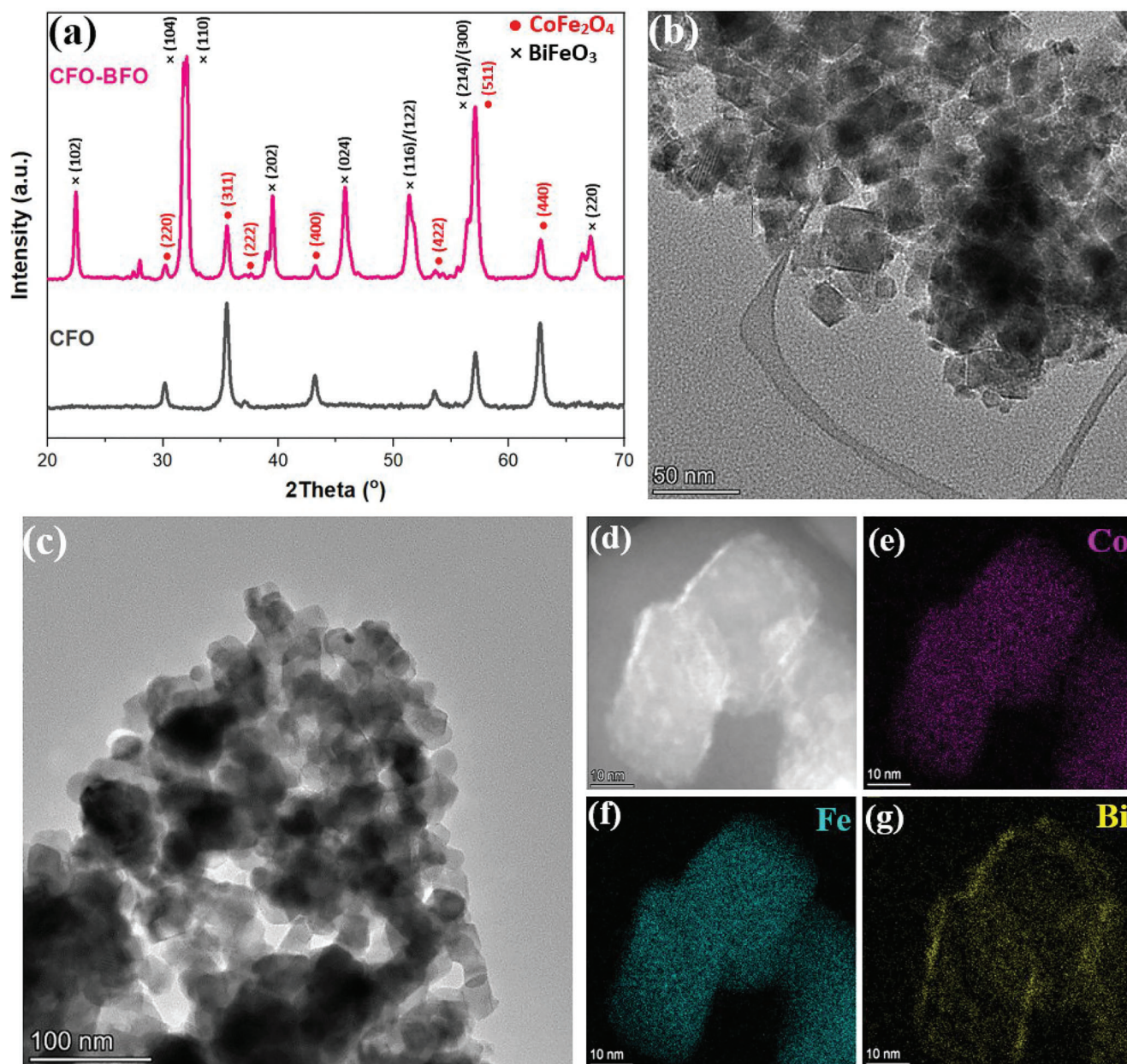
**ADVANCED
SCIENCE NEWS**

www.advancedsciencenews.com

**ADVANCED
MATERIALS
INTERFACES**
Open Access

www.advmatinterfaces.de

Figure 1. Structural analysis of nanoparticles. a) X-ray diffraction (XRD) of as-synthesized CFO core and CFO-BFO core-shell nanoparticles. Each peak corresponds to the Bragg peaks of Fd-3m CFO and R3c BFO phases and no secondary phases nor impurities were observed. TEM images of b) CFO and c) CFO-BFO nanoparticles, respectively. d) High angle annular dark field (HAADF) image of CFO-BFO core-shell nanoparticles and e–g) corresponding EDXS mappings. The core-shell nature of CFO-BFO nanoparticles can be inferred from Co, Fe, and Bi ions distributions.

the interface) due to atomic or lattice discontinuity and modification of chemical bonds, which, in turn, gives rise to different surface potential and WF at the interface. This explanation is consistent with previous works demonstrating that the CFO/BFO interface with a special electronic structure and low energy barrier leads to enhanced local conduction.[47,52] Likewise, the presence of a high density of oxygen vacancies at the CFO/BFO or perovskites/spinels interface can act as donors, facilitating electron transfer to the conduction band. On the other side, the segregation of Fe^{3+} ions in the regions close to the interface can significantly reduce the interfacial energy and increase

the conductivity or electron transfer.[52] Moreover, crystal defects, cation distribution, grain size, porosity, and sintering method can influence the dielectric behavior of ferrite materials.[53] Therefore, the surface potential or electrostatic force signal detected by SKPFM on the CFO-BFO oxide surface is a combination of the surface potential of the BFO shell (a thin layer with an approximate thickness of 5 nm)[24] and the one at the CFO/BFO interface, where the bandgap energy and WF are close to CFO nanoparticles. Based on previous studies,[24,49] the bandgap energies of CFO, BFO, and CFO-BFO nanoparticles were calculated using the Kubelka-Munc function to be 1.45, 2.2, and 1.8 eV,
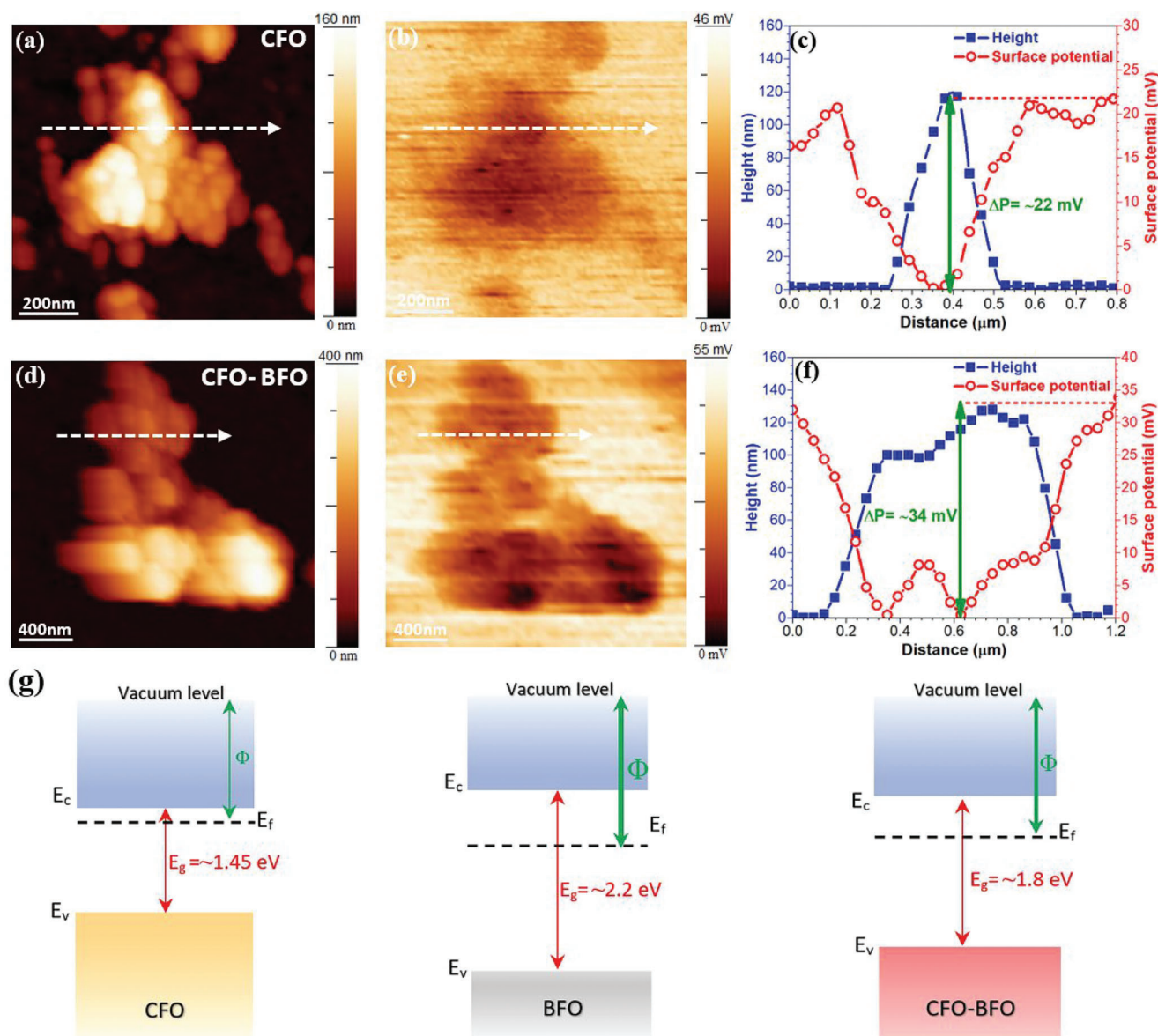
**ADVANCED
SCIENCE NEWS**

www.advancedsciencenews.com

**ADVANCED
MATERIALS
INTERFACES**
Open Access

www.advmatinterfaces.de

Figure 2. AFM, SKPFM images, and corresponding line profiles of a–c) CFO and d–f) CFO-BFO nanoparticles. respectively. g) A schematic representation of the energy band diagram of CFO, BFO, and CFO-BFO oxides.

respectively, considering an approximate CFO core diameter of 20 nm and a BFO shell thickness of 7 nm. Thus, the use of BFO as a coating over CFO results in lower E_g values with respect to bulk BFO. Hence, the difference in surface potential and/or surface charge of CFO and CFO-BFO nanoparticles, $\Delta P_{difference} = \Delta P_{CFO-BFO} - \Delta P_{CFO} = 12$ mV, is not significant because of the close Fermi level values.

According to the above elucidations, we can assume that the charge carrier mobilities (μ) (electron/holes and oxygen vacancies) on the surface oxide of CFO nanoparticles with superior semiconductor behavior is higher than that of CFO-BFO core-shell and BFO nanoparticles ($\mu_{CFO} > \mu_{CFO-BFO} > \mu_{BFO}$, to be shown in the Mott-Schottky results and discussion part). However, we must take into account the relationship between WF and bandgap energy and especially the influence of the WF value

of both nanoparticles on the surface potential difference signal. Due to this fact, the local surface potential difference between the WF of PtIr probe ($\Phi_{PtIr} = 4.28$ eV)[54] and sample (Φ_{sample}) is:[55]

$$\Delta P = \Phi_{PtIr} - \Phi_{sample} / e \qquad (1)$$

Where e is an elementary charge (1.60217×10^{-19} coulombs).

Thus, considering that $\Delta P_{CFO/glassy\ carbon} = 22$ mV and $\Delta P_{CFO-BFO/glassy\ carbon} = 34$ mV, it can be inferred that CFO-BFO nanoparticles show a higher surface potential or WF difference than CFO nanoparticles on glassy carbon. This difference is related to the influence of the BFO shell and the electronic properties of the CFO-BFO interface structure. Materials with high surface potential or WF present higher

stability of valance electrons or a more stable electronic state which inhibits the valence electrons from participating in electrochemical reactions in an environment with various ions and species (complexes, proteins, and cells).[44–46] Consequently, materials with high surface potential or WF value are nobler, and this can serve as a criterion to predict metal ion release or degradation.[56,57]

2.2. Electrochemical Response in PBS at Different pH and Apoferritin Concentrations

Electrochemistry is a valuable tool for studying biodegradation, providing insights into electrochemical reactions and related processes at the material's surface. In this line, OCP measures the potential difference between a degrading material and a reference electrode in the absence of any external applied current, permitting to evaluate its degradation behavior. In the case of CFO and CFO-BFO nanoparticle samples, the OCP evolution was monitored during immersion in the PBS solution with three different pH values (3, 5, and 7) and apoferritin concentrations (0, 10, and 100 µg mL^{-1}) for 1 h at 25 °C and aerated conditions (**Figure 3**a,b). The ITO glass+Nafion® sample exhibits the highest OCP values in PBS solution (≈480 mV vs Ag/AgCl) while the ITO glass is the lowest (−68 mV vs Ag/AgCl) because the Nafion® film can act as a barrier to the diffusion of oxygen, water molecules, and other ions toward the conductive surface of ITO glass.[58,59] This organic layer with hydrophobic behavior increases the electrochemical potential resulting in fewer electrochemical reactions at the solid/organic layer/solution interfaces. In this regard, the OCP curves of both nanoparticles' electrodes are located in between those of both ITO and ITO glass+Nafion® samples. Generally, the CFO-BFO particles present higher OCP values in comparison to the CFO particles in all environmental conditions because of their nobler behavior. Remarkably, a decrease in OCP was recorded for both nanoparticles when decreasing the pH of the solution or increasing the apoferritin concentration.

The degradation or metal ion-releasing process of CFO oxide nanoparticles can be described as:

$$CoFe_2O_4 + 4H_2O \rightarrow 2Fe^{3+} + Co^{2+} + 8\,OH^- \qquad (2)$$
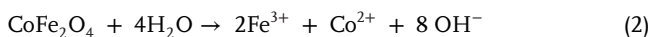
The rate of this reaction is especially dependent on the presence of ion varieties, proteins, cells, and other species, which can accelerate or inhibit the metal ion-releasing process. In the case of apoferritin, its adsorption onto the surface of particles is a quick (seconds to hours)[60] and complex process that significantly impacts the reaction rate. According to previous studies,[61–63] protein molecules during their initial interaction with a solid surface (oxides layer on metal, alloy, and ceramic materials) tend to form a physicochemical metal-protein bond, which acts as a cathodic inhibitor toward reduction reactions (e.g., $2H^+ + 2e^- \rightarrow H_2$ and/or $O_2 + 2H_2O + 4e^- \rightarrow 4OH^-$) and decreases the electrochemical potential. Therefore, a higher concentration of apoferritin molecules provides a stronger effect, resulting in a decrease in the OCP and thus, facilitating the occurrence of anodic reactions.

Anodic reactions were studied by measuring potentiodynamic polarization curves of CFO and CFO-BFO nanoparticle sam-

ples after the OCP measurement (1 h) under environmental conditions (Figure 3c–f). In addition, the electrochemical results of the bare ITO glass and ITO glass+Nafion in PBS and PBS+apoferritin solutions are reported in Figure S4(Supporting Information). In all curves obtained in solutions with pH 7, we can notice a sharp increase in the current density for potentials above 1 V versus Ag/AgCl due to the oxygen evolution reaction (OER). Interestingly, the OER onset potential at pH 7 is lower for CFO than for CFO-BFO (Figure 3d,f) because of the higher electronic conductivity facilitating enhanced charge transfer kinetics in the structure of CFO nanoparticles. Note that these results are in agreement with the ones observed by SKPFM, which indicated a higher WF difference of CFO-BFO nanoparticles alongside a higher E$_g$ value with respect to the CFO nanoparticles. This charge transfer difference is also observed when comparing the anodic current densities of both compounds and is responsible for a slight current reduction when CFO is coated with a BFO shell. In the presence of apoferritin, this anodic current density rises by increasing the protein concentration from 0 up to 100 µg mL^{-1} in both CFO and CFO-BFO nanoparticle samples, indicating the significant role of apoferritin in the degradation process.

Metal ion uptake or release can occur by electron transfer mechanism between the protein shell and the oxide surface.[64] Iron or other metal ions can enter the protein shell through the hydrophilic 3-fold channel and chelate with regions that are enriched by carboxylate-terminated residues.[41,65] Moreover, the adsorption of apoferritin is controlled by electrostatic or hydrophobic interactions on both CFO and CFO-BFO nanoparticles, and is influenced by the charge of the protein molecule and the surface charge on the oxide layer.[41] The electrostatic interaction of proteins with ceramic particles is strongly dependent on the charge distribution and the polar residues of protein structure (isoelectric point (IEP)), which can be controlled by changing the pH.[66] Note that, the IEP of apoferritin protein is reached at a pH between 4.1–5.1.[67,68] Therefore, the apoferritin molecule at pH 3, 5, and 7 exhibits a positive, neutral, and negative zeta potential (ζ), respectively. Also, the apoferritin molecule can maintain its hollow spherical shape with the same structure in the approximate pH range of 7.3 down to 3.[69] Taking into account that the oxide surface of both CFO and CFO-BFO nanoparticles during the overpotential in the anodic region has a positive charge, electrostatic adsorption will occur between the protein and the oxide surface at pH 7. However, at pH 5 and 3, hydrogen bonding and hydrophobic interactions can play a predominant role.[70] As a result, apoferritin molecules cause an increase in the total anodic current density by facilitating the oxidation reactions on the oxide surface of both nanoparticles. Indeed, the adsorption and binding of apoferritin molecules on the oxide surface could accelerate the metal ion release and create defect sites on the surface of CFO and CFO@BFO.

When polarizing the samples to more anodic potentials, we increase the positive surface charge and thus enhance the electrostatic adsorption of apoferritin molecules, which in turn enhance the electron transfer between the ferritin and the oxide surface.[64] Considering that the metal ion up-taking process and the formation of a mineral core by apoferritin shell are based on oxidation reactions, the observed oxidation peaks in the potentiodynamic polarization curves at lower potentials than the OER are
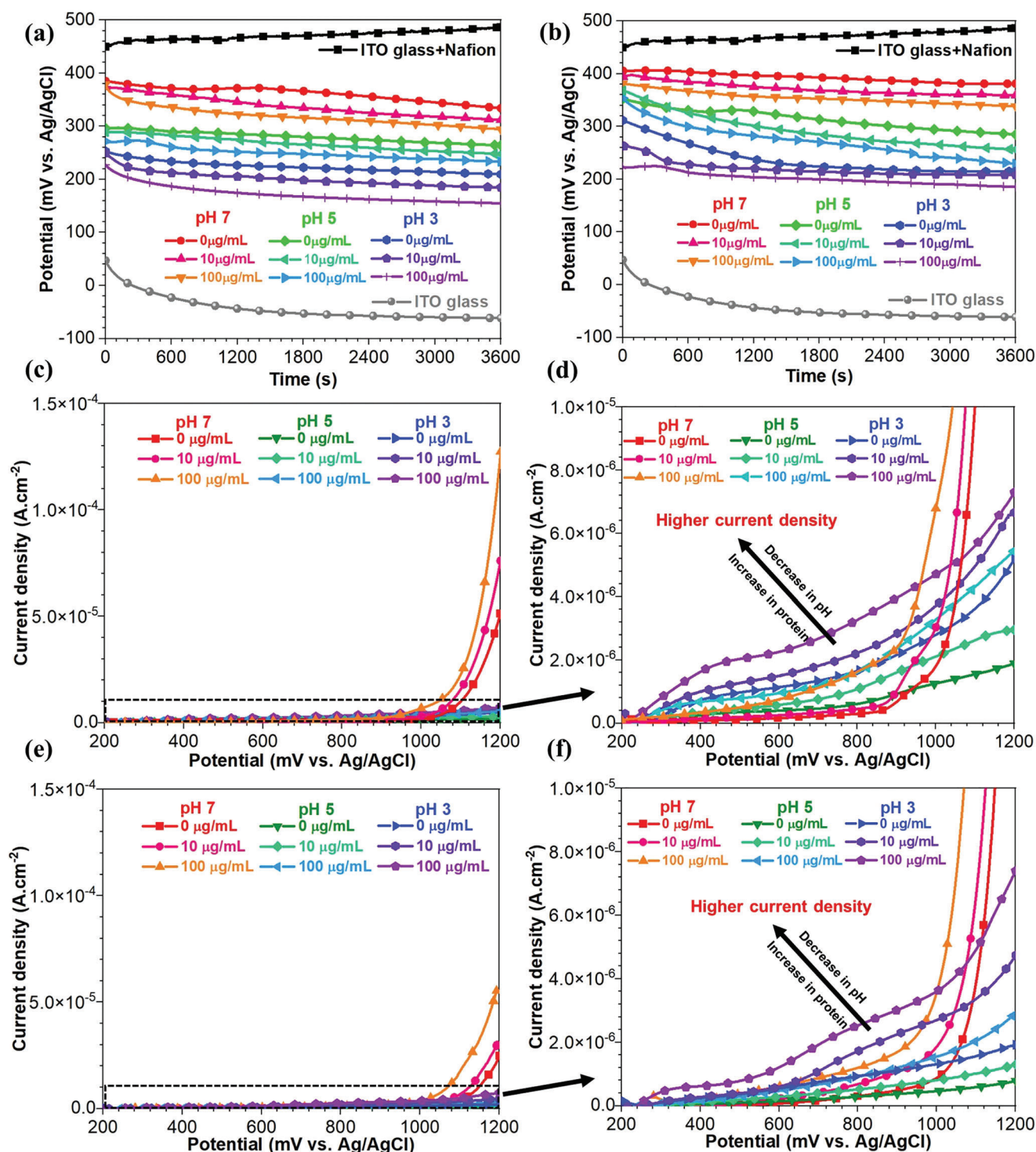
Figure 3. Open-circuit potential (OCP) curves of a) CFO and b) CFO-BFO nanoparticles, I–V curves (anodic potential) of c,d) CFO and e,f) CFO-BFO nanoparticles. All measurements were performed after 1 h immersion in PBS solution with different pH values (3, 5, and 7) and apoferritin protein concentrations (0, 10, and 100 µg mL^{-1}) at 25 °C.

due to the presence of apoferritin. These peaks can be related to multi-reactions/interactions such as protein adsorption and its conformational rearrangements, and complex formation on the oxide surface.[68] In view of the electrochemical results shown in Figure 3, both CFO and CFO-BFO nanoparticle samples present

the highest anodic current density at pH 3 with 100 µg mL^{-1} apoferritin concentration in PBS solution. Thus, the increase in apoferritin concentration and the decrease in pH enhance anodic oxidation reactions, accelerating the degradation of the oxide nanoparticles.
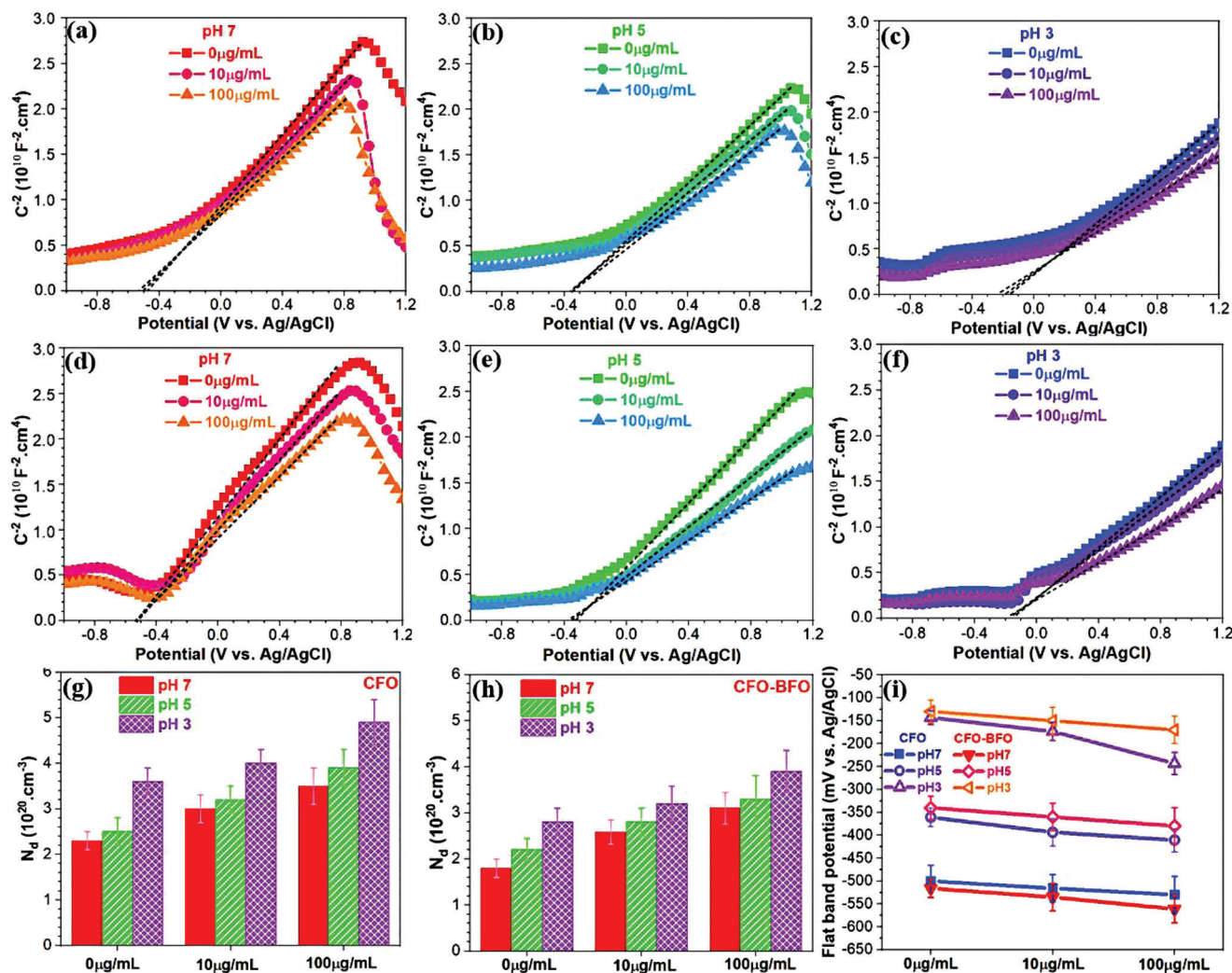
Figure 4. Mott-Schottky analysis of a–c) CFO and d–f) CFO-BFO nanoparticles at different pHs and apoferritin concentrations. Donor charge carriers of g) CFO and h) CFO-BFO nanoparticles, and i) flat band potential values of CFO and CFO-BFO nanoparticles are also summarized.

2.3. Evaluation of Electronic Properties during Interaction with Apoferritin Protein

Apoferritin proteins can interact or bind to metal atoms on the oxide surface of both CFO and CFO-BFO nanoparticles, and this interaction is strongly dependent on the properties of the oxide surface.[71] Thus, the detachment and/or desorption process between varieties of proteins and metal atoms on the oxide surface can occur if the protein-metal bonds at the oxide surface are stronger than metal-oxide (in this case, in bulk) or hydroxide bonds. On this account, we conducted the Mott-Schottky analysis to reveal the type of semiconductor character as well as the role of pH and apoferritin protein molecules on the C^{-2} (space charge region capacitance) magnitude on CFO and CFO-BFO oxide surfaces.

As indicated in **Figure 4**, CFO and CFO-BFO nanoparticle samples in PBS solution with different pH values and apoferritin concentrations showed a positive slope or an increasing trend on C^{-2} value generally for potentials above −0.2 V versus Ag/AgCl. The positive slope with a linear behavior represents an n-type

semiconductor character (N_d, donor density) due to the presence of electrons and oxygen vacancies on the oxide surface of both nanoparticles.[43] In both cases, a decrease in C^{-2} values or a negative slope is observed for solutions with pH 7 and 5 for potentials above 0.9 V versus Ag/AgCl. This behavior can be attributed to the p-type semiconductor character (acceptor density) enriched with hole defects or metal ion vacancies on the oxide surface of the nanoparticles. This effect becomes more pronounced at pH 7 than at pH 5. It has been reported that CFO can act as a semiconductor (electron transfer for conductivity) with n-type or p-type semiconductor characters, which can be attributed to Fe^{2+} (electrons) and Co^{3+} (electron holes), respectively.[48] The main predominant conduction mechanism in $CoFe_2O_4$ is related to the presence of Fe^{2+} and Co^{3+} in octahedral sites:[72]

$$Fe^{3+} + Co^{2+} \leftrightarrow Fe^{2+} + Co^{3+} \qquad (3)$$

In the $BiFeO_3$ shell, the presence of Bi^{3+} in eightfold coordination with ferroelectricity properties and Fe^{3+} in sixfold coordination with magnetism properties provides a favorable

environment for the transfer of charge carriers.[73] The donor density distribution in both nanoparticles clearly explains the role of oxygen vacancies concentration on semiconductor behavior and the charge transfer process during electrochemical reactions on their oxide surface. By reducing the pH value from 7 to 5 and then to 3, both C^{-2} magnitude and the linear regions with positive slopes on CFO and CFO-BFO samples shift to a lower value, slightly more marked on CFO nanoparticle samples. By decreasing the pH to 3, we notice a decrease in the slope of the positive linear region for both the CFO and CFO-BFO particles, which is correlated to an enhancement of the n-type semiconductor character (Figure 4g,h). As depicted in Figure 4i, there is an increase in the higher flat band potential (E_{fb}) for both CFO and CFO-BFO particles when reducing the pH in all apoferritin concentrations. This can be attributed to the protonation/deprotonation process occurring on their oxide surfaces.[74,75]

A high apoferritin concentration (100 µg mL^{-1}) leads to a decrease in the slope of the positive linear region and the p-type semiconductor character onset potential ($\approx$0.8 V vs Ag/AgCl), promoting the formation of defect sites.[43] Additionally, there is a decrease in the E_{fb} value with a higher apoferritin concentration. Increasing the apoferritin concentration from 0 up to 100 µg mL^{-1} enhances the electrochemical interactions, resulting in higher charge transfer, metal-protein detachment, and/or metal ion release.[76] By augmenting the amount of apoferritin, more proteins can interact with the oxide surface and bind with metal atoms on the defect's sites. A previous study showed two main mechanisms that can influence degradation and metal ion release for TiO_2, ZnO, CeO, iron oxides, and aluminum oxides by proteins and other organic substances. These mechanisms include complex formation with metal atoms at the oxide surface or released metal ions and ligand-enhanced dissolution by extracting the metal atoms from the oxide surface.[76] Consequently, apoferritin molecules can facilitate the charge transfer and mass transport at the oxide/protein interface by binding to active sites on the surface oxide and subsequently up-taking or releasing metals such as Fe, Bi, and Co, especially from surface defects (cation vacancies and/or oxygen defects). In this regard, the electrochemical reactions occurring on the oxide surface are strongly dependent on the electron transfer and, in particular, on the donor density. CFO-BFO samples exhibit a slightly higher E_{fb} than CFO samples in all pH and apoferritin concentrations, indicating lower activity and charge carrier densities. Hence, by reducing the donor density (in this case, by using a BFO coating), the electron transfer is decreased and then, the electrochemical reactions can be inhibited, resulting in lower detrimental events.[77]

2.4. Long-Term Biodegradation Monitoring

To gain further insights into the significant impact of both apoferritin molecules and pH on the electrochemical response, as well as the release of Co, Fe, and Bi ions from CFO and CFO-BFO nanoparticles during long-term immersion (maximum 30 days), ICP-AES analysis and impedance/potential evolutions were performed. The reported ICP results indicate that the presence of apoferritin protein at pH 7 and 3 gives rise to a higher release of Co, Fe, and Bi ions from the studied nanoparticles (**Figure 5**a–c).

Notably, the ion release is more intense at pH 3 where a higher rate is detected. In contrast, in the absence of apoferritin, the thin layer of BFO on CFO nanoparticles significantly reduces the release of Fe (2 times decrease at pH 3), and Co (5 times decrease at pH 3) due to its lower electrochemical activity and degradation hindering behavior. However, the addition of apoferritin to the PBS solution triggers the degradation of the BFO nano-coated layer, resulting in an important increase in the concentration of Bi and Fe ions. These ions reach their highest concentration at pH 3, indicating the acceleration of the degradation process at low pH values.

According to the potential versus immersion time curves (Figure 5d), both nanoparticles exhibit a decreasing trend in potential during their interaction with apoferritin molecules for 720 h. Remarkably, CFO-BFO nanoparticles show a slightly higher potential with respect to CFO nanoparticles. Likewise, both oxides display a sharp drop in potential after 8 to 24/48 h and then reach relatively stable values. Regarding the impedance evolution, the modulus value at 0.01 Hz was recorded at different immersion times to extract information about the resistance associated with the charge transfer process on the oxide surface in an apoferritin environment (Figure 5e).[78] In the case of CFO nanoparticles at pH 7, an important increase in resistance after 2 h is observed (565 kΩ cm^2), followed by a slight decrease in the impedance modulus. Then, this value gradually increases up to 48 h (569 kΩ cm^2). For CFO-BFO nanoparticles at pH 7, a sharp rise in impedance modulus value is also detected at the beginning of the immersion (1 h, 456 kΩ cm^2) and continues to increase up to 24 h (668 kΩ cm^2). Both curves evidence a decreasing tendency in impedance value after 48 h. Similar deterioration patterns are observed at pH 3 with apoferritin but with a more detrimental impact.

The variation of the previous values are related to the different steps of the degradation mechanism. At the beginning of immersion, a charging effect occurs on the oxide surface due to the presence of varieties of ions and molecules (Cl$^-$, Na$^+$, H$^+$, OH$^-$, O_2, H_2O), and complex or species (PO_4^-, PO_4^{-3}, apoferritin protein, and metal-protein complex). This charging effect leads to an increase in the charge transfer resistance but reduces the potential value, making degradation thermodynamically more favorable. After a certain time of immersion ($\approx$48 h), the high adsorption of apoferritin molecules on the oxide surfaces leads to a reduction in the OCP and impedance signals as a consequence of the effect of apoferritin on the metal ion release and uptake (Figure 5d,e). The adsorption is controlled by electrostatic or hydrophobic interactions on both CFO and CFO-BFO nanoparticles, and these interactions directly depend on the charge of the protein molecule and the surface charge on the oxide layer. These protein molecules adsorbed on nanoparticles generally evolve dynamically with time as a function of the surrounding physicochemical and biological interactions with the surrounding environment.[79] Consequently, these physicochemical changes at the protein/oxide interface during a long-term period (here until 30 days) can provide appropriate conditions for the detachment process between apoferritin molecules and Bi, Fe, and Co metals from the oxide surface, especially on defects sites.[80] Note that, in this system, metal-protein bonds are expected to be stronger than metal-oxygen bonds, which, in turn, causes more protein-metal complexes to detach, enhancing the release and up-take of metal ions
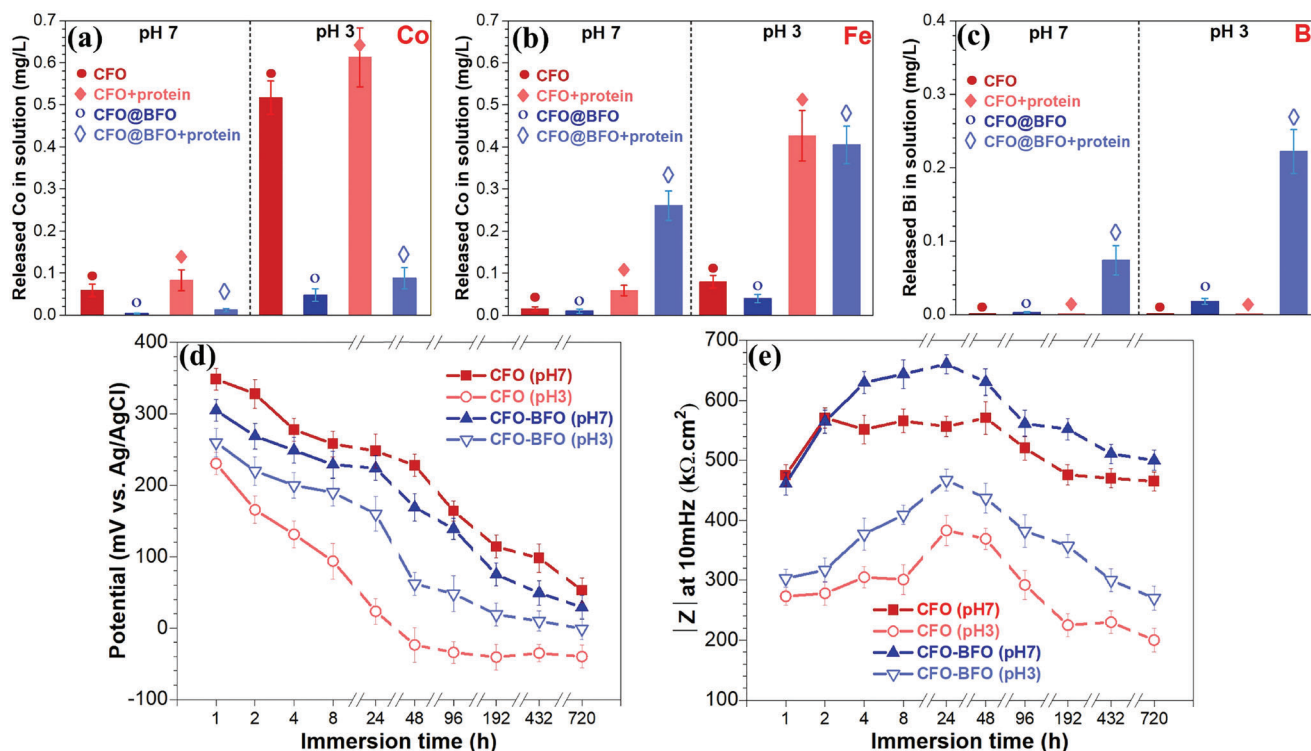
ADVANCED
SCIENCE NEWS

www.advancedsciencenews.com

**ADVANCED
MATERIALS
INTERFACES**
Open Access

www.advmatinterfaces.de

Figure 5. Total amounts of a) Co, b) Fe, and c) Bi-released from CFO and CFO-BFO nanoparticles after 30 days of immersion in the different environmental conditions containing 100 µg mL^{-1} apoferritin at 37 °C. d) OCP and e) impedance modulus value |Z| at 10 mHz during long-term immersion tests of CFO and CFO-BFO nanoparticles in 100 µg mL^{-1} apoferritin media at 37 °C.

mediated by electron transfer mechanism (**Figure 6**).[71] In this regard, given that the presence of a nanometric BFO layer on CFO nanoparticles during exposure to the human body media reduces the electron transfer, it improves the resistance to metal ion-release, hampering the biodegradation process facilitated by apoferritin proteins.

3. Conclusion

In summary, we have studied the electronic properties (at solid/air and solid/electrolyte interfaces by SKPFM and Mott-Schottky analysis, respectively), electrochemical response, and metal ion release of CoFe$_2$O$_4$ (CFO) and CoFe$_2$O$_4$-BiFeO$_3$
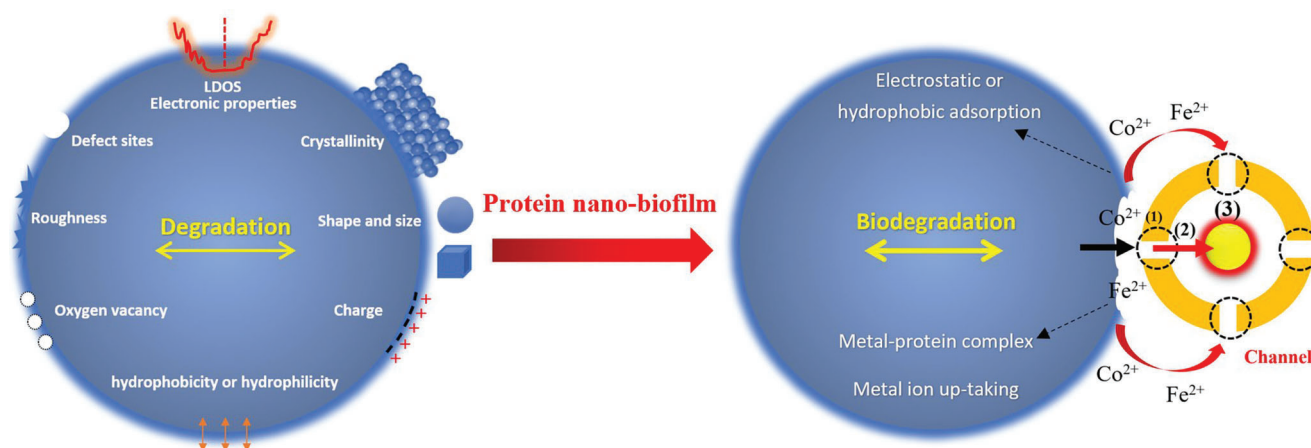

Figure 6. Schematic presentation of CFO material characteristics' role on apoferritin protein adsorption and then its detrimental interactions, particularly its role on metal ion releasing and up-taking processes, Metal ion release and up-take can occur by electron transfer mechanism between the protein shell and the oxide surface.[64] Three consecutive steps proposed in the literature regarding metal ion up-taking process by apoferritin, 1) Metal ions start to binding with the catalytic site of apoferritin in order to initiation of the oxidation process, 2) The bound metal ions are then oxidized (for example Fe (II) to Fe (III)), 3) A binding process can occur with oxidized ions (for example Fe (III)) to nucleation site in the inner protein shell by migration of oxidized ions from oxidation sites.[81]

(CFO-BFO) magnetic nanoparticles in PBS solution containing various concentrations of apoferritin protein and at different pH. SKPFM results revealed a higher surface potential/surface charge difference on CFO-BFO surfaces than CFO, which can be attributed to the electronic properties of the BFO shell and CFO/BFO interface. Through Mott-Schottky analysis, we observed a slightly higher flat band potential and lower donor density distribution on CFO-BFO samples than on CFO in all pH values and apoferritin concentrations, indicating a lower activity with lower charge carrier densities in CFO-BFO nanoparticles. Therefore, a nanometric BFO coating on CFO nanoparticles improves their resistance to metal ion-release during exposure to the human body media. On the other hand, potentiodynamic polarization measurements in different solutions demonstrated higher anodic current densities for both CFO and CFO-BFO samples when decreasing the pH and with 100 µg mL^{-1} apoferritin in PBS solution. The presence of apoferritin increases metal ion release, in particular, Fe (2 times increase at pH 3), and Co (5 times increase at pH 3), contributing to the occurrence of electrochemical reactions and the formation of metal-protein complexes. The long-term monitoring revealed that high apoferritin concentrations and acidic conditions accelerate the biodegradation process of both oxide nanoparticles. This acceleration is demonstrated by the decrease of electrochemical potentials and impedance modulus values, and enhancement of Co, Fe, and Bi ion release. Therefore, these investigations provide new approaches for a systematic understanding of the chemical stability and biodegradation processes of ceramic nanoparticles in human physiological media.

4. Experimental Section

Fabrication of CoFe$_2$O$_4$ and Core-Shell CoFe$_2$O$_4$-BiFeO$_3$ Nanoparticles: CFO nanoparticles were synthesized using co-precipitation and hydrothermal methods.[24] A deionized (DI) water solution of 0.14 M hexadecyltrimethylammonium bromide (CTAB), 0.092 M FeCl$_3$·6H$_2$O, and 0.046 M CoCl$_2$ was prepared and mixed with a 6 M NaOH solution for co-precipitation. Afterward, the solution was sealed in an autoclave and annealed at 180 °C for 24 h. The obtained black powder was washed with DI water and ethanol. Then, the cleansed powder was then dried overnight at 80 °C. BFO shell was synthesized using a sol-gel method. BFO precursor was obtained by preparing 0.011 M Bi(NO$_3$)·5H$_2$O and 0.01 M Fe(NO$_3$)·9H$_2$O in ethylene glycol. Then, 0.1 g of CFO nanoparticles were added and dried overnight, followed by annealing at 600 °C.

Sample Preparation for Electrochemical Measurement: Twenty milligrams of CFO or CFO-BFO were gently mixed with the 150 µL of ethanol and 20 µL of Nafion (Nafion® 117, Sigma–Aldrich).[80,82] Then, the suspension was uniformly coated on 2 × 2cm^2 indium thin oxide (ITO, 18-20 ohms per sq, techinstro) coated glass using a spin coater (Ossila, UK) with a spin speed of 800 rpm and spin time 20 s. Finally, the samples were dried at 60 °C for 1 h. In this condition, the most of top layers or surfaces of nanoparticles have the lowest Nafion influence, while the bottom layers of coated nanoparticles are embedded in the Nafion mixture, as shown in Figure S1 (Supporting Information). The mean value of the thickness and root mean square (RMS) roughness of the nanoparticles-coated layer in all samples were ≈400 and 165 nm, respectively, based on AFM analysis (Figure S2, Supporting Information).

Nanoparticles Characterizations: The crystallinity of the nanoparticles was measured with an X-ray diffractometer (Bruker AXS D8 Advance). Transmission electron microscopy (TEM) and energy dispersive X-ray spectroscopy (EDXS) mapping were measured with FEI Talos F200X. To evaluate the surface potential and work function (WF) distribution,

Scanning Kelvin Probe Force Microscopy (SKPFM, Digital Instruments Nanoscope IIIa) was employed. For atomic force microscopy (AFM) and SKPFM analysis, both CFO and CFO-BFO nanoparticles were mixed with ethanol solution and then uniformly distributed on a glassy carbon plate (VC000502, Goodfellow). The surface potential maps were carried out using the dual-scan mode where topography data was obtained using tapping mode in the first scan while surface potential was obtained in the second scan. Topography and surface potential maps were performed in the air atmosphere at 25 °C with an approximate relative humidity of 28%, a pixel resolution of 512 × 512, a zero-bias voltage, and a scan frequency rate of 0.2 Hz.

Electrolyte and Electrochemical Measurements: The electrochemical and biodegradation behavior of CFO and CFO-BFO nanoparticles were investigated with PBS electrolyte (which composition is: 8 g L^{-1} NaCl, 0.2 g L^{-1} KCl, 1.15 g L^{-1} Na$_2$HPO$_4$, 0.2 g L^{-1} KH$_2$PO$_4$ with a total chloride content 4.94 g L^{-1}) as a simulated body solution in accordance with the ASTM Standard (F2129).[83] Two different concentrations (10 and 100 µg mL^{-1}) of apoferritin (apoferritin from equine spleen, with concentration 100 mg mL^{-1}, 0.2 µm filtered, Sigma–Aldrich) were added to the PBS environment, to provide an inflammatory condition to observe its impact on metal ion release and up-taking processes. Because the pH of electrolytes significantly influences metal ion release and surface charge distributions, three different pH conditions were considered (pH 3, 5, and 7). The pH of the whole solution was carefully controlled by a pH meter (GLP 21, CRISON).[69] All electrochemical measurements were performed at 25 °C and aerated conditions with a potentiostat instrument (AUTOLAB PGSTAT 30) with Ag/AgCl/KCl$_{3M}$ reference electrode (+222 mV vs SHE) and a platinum wire as a counter electrode. The surface area of all exposed samples was carefully controlled to 0.5 cm^2. All electrochemical measurements were performed after 1 h immersion for the stabilization of the open circuit potential (OCP). Potentiodynamic polarization measurements were carried out at a scan rate of 1 mV s^{-1} at anodic potentials to study the oxidation or anodic reaction kinetics on the oxide nanoparticle surfaces for both CFO and CFO-BFO. For the long-term electrochemical analysis, CFO and CFO-BFO nanoparticles were immersed in a PBS solution with an apoferritin concentration of 100 µg mL^{-1} for 30 days and monitored by electrochemical impedance spectroscopy (EIS) with a frequency range of 10 mHz to 100 kHz, applying a sinusoidal excitation signal of ±10 mV at OCP condition (Bode data are reported in Figure S3, Supporting Information). Mott-Schottky analysis was performed at 1 kHz frequency in the potential range of −1 to 1.2 V versus Ag/AgCl with an amplitude value of ±10 mV (more information can be found in Supporting information).

Long-Term Approaches for Nanoparticles Biodegradation Tests: For long-time degradation behavior observations, both CFO and CFO-BFO nanoparticles were dispersed in PBS and PBS + 100 µg mL^{-1} apoferritin environments in the two different pH values (3 and 7) at 37 °C for 30 days (in a dark chamber). After carefully removing the nanoparticles, all solutions were properly prepared using the acid digestion process before starting the inductively coupled plasma-atomic emission spectrometry (ICP-AES, Agilent 5800) analysis to detect the released Co, Fe, and Bi ions. The digestion process was performed on a hot plate in a beaker by adding 2 mL of HNO$_3$ (65% Merck) and 2 mL of H$_2$O$_2$ (PanReac Applichem, 30% w/v (100 vol)).[84]

Statistical Analysis: Each data point in the metal ion release and impedance/potential monitoring experiments was measured at least three times. The data were presented as mean ± SD.

Supporting Information

Supporting Information is available from the Wiley Online Library or from the author.

Acknowledgements

Conflict of Interest

The authors declare no conflict of interest.

Data Availability Statement

The data that support the findings of this study are available from the corresponding author upon reasonable request.

Keywords

[1] D. Ling, T. Hyeon, *Small* **2013**, *9*, 1450.
[2] D. L. Huber, *Small* **2005**, *1*, 482.
[3] V. Georgiadou, G. Makris, D. Papagiannopoulou, G. Vourlias, C. Dendrinou-Samara, *ACS Appl. Mater. Interfaces* **2016**, *8*, 9345.
[4] N. Sanpo, C. C. Berndt, C. Wen, J. Wang, *Acta Biomater.* **2013**, *9*, 5830.
[5] P. M. Price, W. E. Mahmoud, A. A. Al-Ghamdi, L. M. Bronstein, *Front. Chem.* **2018**, *6*, 619.
[6] K. Ulbrich, K. Holá, V. Šubr, A. Bakandritsos, J. Tuček, R. Zbořil, *Chem. Rev.* **2016**, *116*, 5338.
[7] A. M. Matos, A. I. Gonçalves, A. J. El Haj, M. E. Gomes, *Nanoscale Adv.* **2020**, *2*, 140.
[8] L. J. Santos, R. L. Reis, M. E. Gomes, *Trends Biotechnol.* **2015**, *33*, 471.
[9] D. Fan, Q. Wang, T. Zhu, H. Wang, B. Liu, Y. Wang, Z. Liu, X. Liu, D. Fan, X. Wang, *Front. Chem.* **2020**, *8*, 745.
[10] Z. W. Tay, P. Chandrasekharan, A. Chiu-Lam, D. W. Hensley, R. Dhavalikar, X. Y. Zhou, E. Y. Yu, P. W. Goodwill, B. Zheng, C. Rinaldi, *ACS Nano* **2018**, *12*, 3699.
[11] K. E. Scarberry, E. B. Dickerson, J. F. McDonald, Z. J. Zhang, *J. Am. Chem. Soc.* **2008**, *130*, 10258.
[12] C. Zhang, W. Bu, D. Ni, S. Zhang, Q. Li, Z. Yao, J. Zhang, H. Yao, Z. Wang, J. Shi, *Angew. Chem.* **2016**, *128*, 2141.
[13] M. Bañobre-López, A. Teijeiro, J. Rivas, *Rep. Pract. Oncol. Radiother.* **2013**, *18*, 397.
[14] Q. Zhang, T. Yin, G. Gao, J. G. Shapter, W. Lai, P. Huang, W. Qi, J. Song, D. Cui, *ACS Appl. Mater. Interfaces* **2017**, *9*, 17777.
[15] B. R. Smith, S. S. Gambhir, *Chem. Rev.* **2017**, *117*, 901.
[16] G. Liu, J. Gao, H. Ai, X. Chen, *Small* **2013**, *9*, 1533.
[17] N. Kolishetti, A. Vashist, A. Y. Arias, V. Atluri, S. Dhar, M. Nair, *Mol. Aspects Med.* **2022**, *83*, 101046.
[18] S. Kopyl, R. Surmenev, M. Surmeneva, Y. Fetisov, A. Kholkin, *Mater. Today Bio* **2021**, *12*, 100149.
[19] F. Mushtaq, H. Torlakcik, Q. Vallmajo-Martin, E. C. Siringil, J. Zhang, C. Röhrig, Y. Shen, Y. Yu, X.-Z. Chen, R. Müller, *Appl. Mater. Today* **2019**, *16*, 290.
[20] F. Zan, Y. Ma, Q. Ma, Y. Xu, Z. Dai, G. Zheng, M. Wu, G. Li, *J. Am. Ceram. Soc.* **2013**, *96*, 3100.
[21] D. Chen, X. Yi, Z. Chen, Y. Zhang, B. Chen, Z. Kang, *Int. J. Appl. Ceram. Technol.* **2014**, *11*, 954.
[22] C. P. Fernández Perdomo, F. L. Zabotto, D. Garcia, R. H. Kiminami, *Int. J. Appl. Ceram. Technol.* **2019**, *16*, 2073.
[23] S. Ayyappan, J. Philip, B. Raj, *J. Phys. Chem. C* **2009**, *113*, 590.
[24] F. Mushtaq, X. Chen, H. Torlakcik, C. Steuer, M. Hoop, E. C. Siringil, X. Marti, G. Limburg, P. Stipp, B. J. Nelson, *Adv. Mater.* **2019**, *31*, 1901378.
[25] X.-M. Liu, S.-Y. Fu, C.-J. Huang, *Mater. Sci. Eng., B* **2005**, *121*, 255.
[26] J. Mosayebi, M. Kiyasatfar, S. Laurent, *Adv. Healthcare Mater.* **2017**, *6*, 1700306.
[27] V. F. Cardoso, A. Francesko, C. Ribeiro, M. Bañobre-López, P. Martins, S. Lanceros-Mendez, *Adv. Healthcare Mater.* **2018**, *7*, 1700845.
[28] C. Fang, N. Bhattarai, C. Sun, M. Zhang, *Small* **2009**, *5*, 1637.
[29] M. Levy, N. Luciani, D. Alloyeau, D. Elgrabli, V. Deveaux, C. Pechoux, S. Chat, G. Wang, N. Vats, F. Gendron, *Biomaterials* **2011**, *32*, 3988.
[30] S. Novak, D. Drobne, M. Golobič, J. Zupanc, T. Romih, A. Gianoncelli, M. Kiskinova, B. Kaulich, P. Pelicon, P. Vavpetič, *Environ. Sci. Technol.* **2013**, *47*, 5400.
[31] Z. Sun, V. Yathindranath, M. Worden, J. A. Thliveris, S. Chu, F. E. Parkinson, T. Hegmann, D. W. Miller, *Int. J. Nanomed.* **2013**, *8*, 961.
[32] F. Ahmad, H. Yao, Y. Zhou, X. Liu, *Chemosphere* **2015**, *139*, 479.
[33] M. Safi, M. Yan, M.-A. Guedeau-Boudeville, H. Conjeaud, V. Garnier-Thibaud, N. Boggetto, A. Baeza-Squiban, F. Niedergang, D. Averbeck, J.-F. Berret, *ACS Nano* **2011**, *5*, 5354.
[34] J. Volatron, F. Carn, J. Kolosnjaj-Tabi, Y. Javed, Q. L. Vuong, Y. Gossuin, C. Ménager, N. Luciani, G. Charron, M. Hémadi, *Small* **2017**, *13*, 1602030.
[35] G. Stepien, M. Moros, M. Pérez-Hernández, M. Monge, L. Gutiérrez, R. M. Fratila, M.d. l. Heras, S. Menao Guillen, J. J. Puente Lanzarote, C. Solans, *ACS Appl. Mater. Interfaces* **2018**, *10*, 4548.
[36] J. Kolosnjaj-Tabi, Y. Javed, L. Lartigue, J. Volatron, D. Elgrabli, I. Marangon, G. Pugliese, B. Caron, A. Figuerola, N. Luciani, *ACS Nano* **2015**, *9*, 7925.
[37] M. Geppert, M. C. Hohnholt, S. Nürnberger, R. Dringen, *Acta Biomater.* **2012**, *8*, 3832.
[38] A. Van de Walle, A. P. Sangnier, A. Abou-Hassan, A. Curcio, M. Hemadi, N. Menguy, Y. Lalatonne, N. Luciani, C. Wilhelm, *Proc. Natl. Acad. Sci. USA* **2019**, *116*, 4044.
[39] J. Volatron, J. Kolosnjaj-Tabi, Y. Javed, Q. L. Vuong, Y. Gossuin, S. Neveu, N. Luciani, M. Hémadi, F. Carn, D. Alloyeau, *Sci. Rep.* **2017**, *7*, 40075.
[40] E. C. Theil, T. Tosha, R. K. Behera, *Acc. Chem. Res.* **2016**, *49*, 784.
[41] M.-S. Pyon, R. J. Cherry, A. J. Bjornsen, D. C. Zapien, *Langmuir* **1999**, *15*, 7040.
[42] D. Kim, K. Shin, S. G. Kwon, T. Hyeon, *Adv. Mater.* **2018**, *30*, 1802309.
[43] E. Rahimi, R. Offoiach, M. Lekka, L. Fedrizzi, *Colloids Surf., B* **2022**, *212*, 112346.
[44] M. Rohwerder, F. Turcu, *Electrochim. Acta* **2007**, *53*, 290.
[45] E. Rahimi, A. Rafsanjani-Abbasi, A. Imani, A. Davoodi, *Mater. Chem. Phys.* **2018**, *212*, 403.
[46] C. Örnek, C. Leygraf, J. Pan, *Corros. Eng., Sci. Technol.* **2019**, *54*, 185.
[47] Y. Zhao, J. Li, Z. Yin, X. Zhang, J. Huang, L. Cao, H. Wang, *J. Alloys Compd.* **2020**, *823*, 153699.
[48] G. Jonker, *J. Phys. Chem. Solids* **1959**, *9*, 165.
[49] F. Mushtaq, X. Chen, H. Torlakcik, B. J. Nelson, S. Pané, *Nano Res.* **2020**, *13*, 2183.
[50] R. Panda, D. Behera, *J. Alloys Compd.* **2014**, *587*, 481.
[51] E. Rahimi, R. Offoiach, S. Hosseinpour, A. Davoodi, K. Baert, A. Lutz, H. Terryn, M. Lekka, L. Fedrizzi, *Appl. Surf. Sci.* **2021**, *563*, 150364.
[52] Y. H. Hsieh, J. M. Liou, B. C. Huang, C. W. Liang, Q. He, Q. Zhan, Y. P. Chiu, Y. C. Chen, Y. H. Chu, *Adv. Mater.* **2012**, *24*, 4564.
[53] N. Sheoran, V. Kumar, A. Kumar, *J. Magn. Magn. Mater.* **2019**, *475*, 30.
[54] S. Sadewasser, T. Glatzel, M. Rusu, A. Jäger-Waldau, M. C. Lux-Steiner, *Appl. Phys. Lett.* **2002**, *80*, 2979.

**ADVANCED
SCIENCE NEWS**

www.advancedsciencenews.com

**ADVANCED
MATERIALS
INTERFACES**

www.advmatinterfaces.de

[55] A. Liscio, V. Palermo, P. Samorì, *Acc. Chem. Res.* **2010**, *43*, 541.

[56] E. Rahimi, A. Kosari, S. Hosseinpour, A. Davoodi, H. Zandbergen, J. M. C. Mol, *Appl. Surf. Sci.* **2019**, *496*, 143634.

[57] E. Rahimi, A. Rafsanjani-Abbasi, A. Imani, S. Hosseinpour, A. Davoodi, *Corros. Sci.* **2018**, *140*, 30.

[58] T. Mashio, K. Malek, M. Eikerling, A. Ohma, H. Kanesaka, K. Shinohara, *J. Phys. Chem. C* **2010**, *114*, 13739.

[59] D. K. Paul, K. Karan, A. Docoslis, J. B. Giorgi, J. Pearce, *Macromolecules* **2013**, *46*, 3461.

[60] M. H. Wood, C. G. Payagalage, T. Geue, *J. Phys. Chem. B* **2018**, *122*, 5057.

[61] H.-H. Huang, *Biomaterials* **2003**, *24*, 275.

[62] Y. Yan, H. Yang, Y. Su, L. Qiao, *Sci. Rep.* **2015**, *5*, 18403.

[63] I. Milošev, *Biomedical Applications*, Springer, New York **2012**, pp. 1–72.

[64] R. J. Cherry, A. J. Bjornsen, D. C. Zapien, *Langmuir* **1998**, *14*, 1971.

[65] J. Kolay, S. Bera, T. Rakshit, R. Mukhopadhyay, *Langmuir* **2018**, *34*, 3126.

[66] K. Rezwan, L. P. Meier, M. Rezwan, J. Vörös, M. Textor, L. J. Gauckler, *Langmuir* **2004**, *20*, 10055.

[67] L. Stühn, J. Auernhammer, C. Dietz, *Sci. Rep.* **2019**, *9*, 17755.

[68] M. Tominaga, A. Ohira, Y. Yamaguchi, M. Kunitake, *J. Electroanal. Chem.* **2004**, *566*, 323.

[69] M. Kim, Y. Rho, K. S. Jin, B. Ahn, S. Jung, H. Kim, M. Ree, *Biomacromolecules* **2011**, *12*, 1629.

[70] A. G. Hemmersam, K. Rechendorff, F. Besenbacher, B. Kasemo, D. S. Sutherland, *J. Phys. Chem. C* **2008**, *112*, 4180.

[71] Y. S. Hedberg, *npj Mater. Degrad.* **2018**, *2*, 26.

[72] A. Hossain, M. Sarker, M. Khan, F. Khan, M. Kamruzzaman, M. Rahman, *Appl. Phys. A* **2018**, *124*, 608.

[73] G. Catalan, J. F. Scott, *Adv. Mater.* **2009**, *21*, 2463.

[74] J. M. Bolts, M. S. Wrighton, *J. Phys. Chem.* **1976**, *80*, 2641.

[75] J. Bandara, R. A. S. S. Ranasinghe, *Appl. Catal., A* **2007**, *319*, 58.

[76] A. E. Nel, L. Mädler, D. Velegol, T. Xia, E. M. Hoek, P. Somasundaran, F. Klaessig, V. Castranova, M. Thompson, *Nat. Mater.* **2009**, *8*, 543.

[77] G. Ou, F. Wu, K. Huang, N. Hussain, D. Zu, H. Wei, B. Ge, H. Yao, L. Liu, H. Li, *ACS Appl. Mater. Interfaces* **2019**, *11*, 3978.

[78] S. Fan, W. Wang, H. Ke, Y. Zhou, *Part. Part. Syst. Charact.* **2018**, *35*, 1800223.

[79] B.-J. L. Van Hong Nguyen, *Int. J. Nanomed.* **2017**, *12*, 3137.

[80] E. Rahimi, R. Offoiach, S. Deng, X. Chen, S. Pané, L. Fedrizzi, M. Lekka, *Appl. Mater. Today* **2021**, *24*, 101135.

[81] B. G. Goldner, A. L. Rinehart, H. M. Benshoff, D. C. Harris, *Biochim. Biophys. Acta, Gen. Subj.* **1982**, *719*, 641.

[82] X. Zhao, Y. Fu, J. Wang, Y. Xu, J.-H. Tian, R. Yang, *Electrochim. Acta* **2016**, *201*, 172.

[83] A. F-06, *Standard Test Method for Conducting Cyclic Potentiodynamic Polarization Measurements to Determine the Corrosion Susceptibility of Small Implant Devices*, ASTM International, West Conshohocken, PA **2001**.

[84] S. Karimi, T. Nickchi, A. M. Alfantazi, *Appl. Surf. Sci.* **2012**, *258*, 6087.